Flow Structure Past a Canonical Shape of Engine/Pylon/Wing Installation for Takeoff/Landing Conditions

Matthieu Lucas* and Yannick Bury†
University of Toulouse, ISAE-SUPAERO, 31055 Toulouse, France
and
Cyril Bonnaud‡
Airbus Operation SAS, 31060 Toulouse, France

https://doi.org/10.2514/1.J058426

Here, a canonical model is proposed, which is able to represent the flow past a wing equipped with a pylon-mounted engine at low speed/moderate angle of attack. The vortices that develop past this model are described numerically and experimentally. For such configurations, the presence of a power-plant installation under the wing initiates a complex and unsteady vortical flowfield at the nacelle/pylon/wing junctions, responsible for a drop in aircraft performances. To gain insight into the underlying physics, the geometry is simplified into a symmetric *two-dimensional* extruded wing equipped with a symmetric, hemispheric-ended cylinder. The study was conducted at a Reynolds number of 200,000, based on the wing chord and on the freestream velocity. Two angle of attack α/sideslip angle β configurations are investigated on the basis of unsteady Reynolds-averaged Navier–Stokes computations, oil-flow visualizations, and stereoscopic particle image velocimetry. The vortex dynamics thus produced is described in terms of vortex core position, intensity, and size. The analysis of the velocity flowfields obtained from the wind-tunnel measurements and the numerical computations highlights the influence of the longitudinal vortex initiated at the pylon/wing junction on the separation process of the boundary layer near the upper-wing leading edge.

Nomenclature

c	=	wing chord length, m
dt	=	computational time step, s
R	=	vortex core radius, m
Re_c	=	Reynolds number based on International Standard Atmosphere conditions, freestream velocity V_∞, and c
V_∞	=	freestream velocity, m/s
x	=	streamwise direction in the wind-tunnel reference frame, m
y	=	spanwise direction in the wind-tunnel reference frame, m
y_c	=	vortex centroid y position, m
z_c	=	vortex centroid z position, m
α	=	angle of attack, deg
β	=	sideslip angle, deg
Γ	=	vortex circulation, m^2/s
ω_x	=	streamwise vorticity, /s

I. Introduction

OVER the past few years, the design of a power-plant installation, composed of the engine, nacelle, and pylon, mounted below or over the wing [1], has become a crucial phase in the development of commercial aircraft [2–5]. From an aerodynamic point of view, the design of the pylon and nacelle results from a compromise between minimizing the drag of the power-plant installation at the optimal cruise point [6–10] and guaranteeing a safe aircraft behavior in the whole flight domain [11,12]. In parallel, the improvement of aircraft performances, in particular, in terms of noise mitigation and reduction of pollutant emissions, prompts engine manufacturers to increase the engine bypass ratio, and consequently, their diameters [13]. Notably, because of runway clearance constraints, these high-bypass-ratio (HBR) engines are set up closer to the wing than the previous transport aircraft generation. Such designs, hereafter denoted as *close coupled*, promote a stronger and more complex aerodynamic interaction between the engine nacelle and the wing, both for cruise flight conditions, in which unsteady interference may affect the aeroelastic stability of the aircraft [14], but also during the takeoff and landing phases, in which the aircraft is operating at a moderate, or even a relatively high, angle of attack. During these particular flight phases, the power-plant-to-wing proximity promotes the occurrence of a complex vortex dynamics at the junction between the nacelle, the pylon, and the wing, which is advected along the upper wing [15]. The interaction of these vortices with the boundary layer on the suction side of the wing can lead to local flow separation [15–17], responsible for a drop in aircraft aerodynamic performances [18,19] and a potential premature stall mechanism [20].

During the past 12 years, three major research programs have partly addressed this complex dynamics: the European High Lift Programme II (EUROLIFT II) [18,21,22], a Japan Aerospace Exploration Agency Standard Model (JAXA JSM) research program [17,19,20,23], and the Reference Experiments for Nacelle Integration (RENI) project [24].

The EUROLIFT II project and the JAXA research program focused on the maximum lift operating point for a high-lift aircraft configuration. In particular, one of the main objectives of the EUROLIFT II project was to improve the understanding of the development of different vortices and their interaction with the flowfield that develops past high-lift geometry. Indeed, such an interaction is one of the principal causes of Reynolds-number effect on the maximum lift [18]. To this avail, Reynolds-averaged Navier–Stokes (RANS) computations and wind-tunnel (WT) measurements were conducted on three geometries of increasing complexity, up to a realistic configuration of a modern commercial aircraft in high-lift configuration, equipped with a nacelle strake. The Reynolds number, based on the chord length of the wing and the freestream velocity, ranged from $Re = 1.5 \times 10^6$ to $Re = 25 \times 10^6$. Despite the highlighted Reynolds-number dependency on global aerodynamic coefficients, stall mechanisms were revealed to be similar in this large Reynolds-number range, whatever the considered geometry [25]. The vortex dynamics was partially described to analyze these mechanisms. It is shortly recalled here. Indeed, for the configuration without a strake, a strong nacelle vortex, similar to the one identified in the RENI project [24] and noted

*Ph.D. Student, ISAE-Supaéro, Department of Aerodynamics, Energetics and Propulsion.
†Associate Professor, ISAE-Supaéro, Department of Aerodynamics, Energetics and Propulsion; yannick.bury@isae.fr. Senior Member AIAA.
‡Group Leader, Department of Aerodynamics for Powerplant Integration.

C in Sec. II, was observed. By increasing the angle of attack, the flow separation that initially developed close to the pylon, at the inboard slat leading edge, progressively promoted a trailing-edge separation of the main wing. Consecutively, a lift decrease was initiated by the growing of the wing-root separation. As the nacelle strake was added, approximately 60% of the loss of the maximum lift was recovered. The strake generated a vortex that interacted with the nacelle vortex. The local flow separation at the leading edge was then strongly mitigated and stall mechanism is now dominated by an outboard separation mechanism on the main wing.

Within the JAXA research program, a detailed flow database for the prediction of lift performance on an actual aircraft configuration was acquired by means of experiments and computations, and for two types of close-coupled nacelle configuration fixed to the wing with a flattened crest pylon: a long-cowling nacelle and a short-cowling nacelle [19]. For a high angle of attack, a longitudinal pylon vortex was observed. This vortex affected the flow downstream of the slat-cutoff region and on the main wing [17], thus reducing the lift performance. Similarly to the EUROLIFT II project results, this loss of lift was mitigated when the strake, namely, here, *chine*, was correctly positioned on the nacelle. A design process using a kriging surrogate model was proposed for this purpose [23].

In the RENI project, a collaborative work between Institut Supérieur de l'Aéronautique et de l'Espace (ISAE) and Airbus has been performed, both experimentally and numerically, to gain insight into the flowfield that develops around and in the wake of the power-plant installation at a low speed and a moderate angle of attack. The reference model considered in the RENI project was a 1 : 22nd scaled half-wing of an existing four-engine commercial aircraft with retracted high-lift systems, equipped with a symmetric pylon linking the nacelle to the wing. This configuration is illustrated in Figs. 1a and 4. WT experiments consisted in longitudinal and transverse to freestream particle image velocimetry (PIV) measurement planes at various locations along the suction side of the wing, downstream of the power-plant installation. These quantitative measurements were complemented with oil-flow visualizations for the determination of the skin-friction line patterns. The results revealed a complex and unsteady vortex dynamics interacting with the upper-wing boundary layer. Three main vortices were characterized in terms of vortex core position, size, intensity, and fluctuation levels, thanks to an in-house vortex tracking algorithm applied on the PIV database [26]. The scenario of this vortex network dynamics is briefly recalled in Sec. II.

More recently, Schindler et al. [15] reported the occurrence of two vortices on the upper part of the pylon and on the inner side of the nacelle, respectively. Despite the high-lift systems deployed and the different Reynolds number in comparison with the RENI configuration, a similar vortex dynamics was reported in this study. In particular, the location of the tornadolike vortex, whose inception was clearly identified by a focus associated with a local drop in the pressure coefficient on the upper part of the pylon, near the wing leading edge, was analogous to the one reported in the RENI project [24] (see Sec. II).

Through these projects, the global impact of ultra-HBR [(U)HBR] power-plant integration on the aerodynamic performances of a wing has been addressed. However, there is still a lack of thorough understanding and characterization of the complex vortex dynamics issued from the junction of the nacelle, the pylon, and the wing during low-speed/moderate-to-high incidence flight phases.

It has been shown that a network of at least two counter-rotating vortices is initially generated at the junction between the nacelle, the pylon, and the leading edge of the wing. The proximity of the wall and the adverse pressure gradient promoted by the suction side of the wing, even if moderate, do most probably affect the dynamics and evolution of these vortices, in addition to the possible vortex/vortex interaction, following complex intrinsic mechanisms.

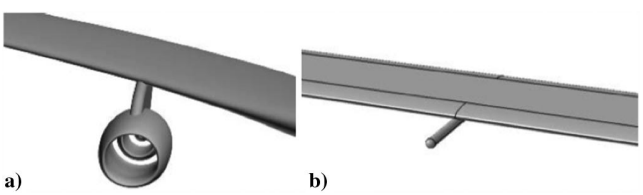

Fig. 1 Power-plant installation of a) the RENI model and b) the simplified geometry.

Previous studies have investigated the interaction of a primary vortex or a pair of counter-rotating vortices with a wall and with a wall-bounded shear layer [27–30]. They revealed its strong influence on the production of turbulent kinetic energy and shear stress levels in both the boundary layer and the vortex cores. They also highlighted the occurrence of short-wavelength elliptic instabilities in the secondary vortex, which affect the primary vortex as the Reynolds number is increased. However, these studies were essentially conducted in a quiescent fluid or in the presence of a weak head- or crosswind.

In the presence of an adverse pressure gradient, as the one imposed on the suction side of the wing, a vortex may experience a so-called breakdown phenomenon. Although the variety of technical applications, in which it is, voluntarily or not, involved and despite numerous researches since the early 1960s [31–34], the vortex breakdown phenomenon still suffers a lack of comprehension. Ruith et al. [35], in their study about the three-dimensional (3-D) vortex breakdown in swirling jets and wakes, have partly addressed this issue. In particular, they have shown that highly rotational flows at large Reynolds numbers could exhibit various breakdown modes, referred to as bubble, helical, or double helical. The influence of a jetlike and wakelike axial velocity profile was also investigated and revealed to promote the axisymmetric mode in the case of a jetlike vortex or nonaxisymmetric breakdown modes for a wakelike vortex.

In the applicative and industrial context of (U)HBR power-plant integration, one can expect that all or part of these instabilities, or at least their firstfruits, give rise to an unsteady flow, as already revealed in the RENI project [24], for instance. But, to date, the way these instability-based mechanisms may interact, and their relative weights in the generation of an unsteady flow, is still difficult, if not impossible, to evaluate.

In an attempt to unravel this complex flow dynamics, it is initially proposed in this study to simplify the geometry of the nacelle/pylon/wing configuration of a real transport aircraft by isolating some fundamental mechanisms responsible for the resulting vortical flow. The parameters of interest that led to the simplification of the model are first described. This study is then conducted on the basis of complementary stereoscopic PIV measurements (3C-PIV), oil-flow visualizations, and unsteady RANS (URANS) computations. Several WT model angles of attack α and sideslip angles β are investigated, aiming at progressively recovering the vortical flow observed on an actual aircraft configuration.

Therefore, the objectives of the current investigation are twofold: first, to decipher the vortex dynamics around a simplified geometry in terms of vortex core position, intensity, and size; second, to gain a better insight into the influence of the longitudinal vortex, originating at the pylon/wing intersection, on the separation process of the boundary layer near the upper-wing leading edge.

Considering this study in an applicative light, and, in particular, in the context of a power-plant integration and its impact on flight performance, the response time of the structure is far below the characteristic timescales associated with the potential previously mentioned instabilities. It is most probably essentially sensitive to the mean flow and "feels" any temporal variation of the flow at a given location on the suction side of the wind and in its close wake, whatever its origin—meander, vortex breakdown, boundary layer, and wake turbulence—as fluctuations. As such, and because this is of practical interest for the applicative concerns considered here, meandering, vortex potential breakdown, and any other flow instability will be considered as contributive parts of the flow fluctuations and will be included in the terminology *fluctuations*, on an equal level with boundary layer or wake turbulence. In this context, and to guarantee the pertinence of the computational fluid dynamics (CFD) vs experiments comparison, the analysis will be based on time-averaged flowfields.

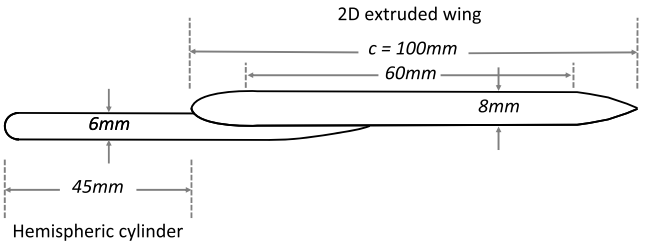

Fig. 2 Two-dimensional schematic of the simplified geometry.

II. Definition of the Simplified Model

On the basis of the RENI project experimental and numerical databases, a simplification of the model is proposed. The reader can refer to [36] for an exhaustive description of the simplification process of this model. This new simplified geometry, illustrated in Figs. 1b and 2, is composed of a symmetric wing with a chord length c equal to 0.1 m and a wingspan equal to 0.7 m. A hemispheric cylinder replaced the symmetric pylon. Its position coincides with one of the original pylons. The cylinder length is 45 mm up to the wing leading edge. Its diameter is equal to 6 mm. The hemispheric part was chosen to simplify the computational meshing process. To impose a leading-edge-induced suction similar to the one generated on the upper wing of the RENI model (Fig. 1a), their curvatures were identically designed. The original RENI cambered wing, optimized for cruise speed, promotes a nonuniform pressure gradient on the suction side of the wing, making the analysis of the interaction between the upper-wing boundary layer and the vortices more complex. Therefore, the central part of the simplified model was reduced to a flat part of constant thickness equal to 8 mm and of chord length equal to 60 mm. This maintained a constant pressure gradient along this flat part for a given angle of attack [36]. Finally, the new geometry design was progressively closed up to a 0.4-mm-thick trailing edge.

Because the simplified geometry should restore a close-to-wall vortex dynamics representative of the one actually observed on a (U) HBR power-plant-equipped wing, the latter was further documented with additional experimental and computational results derived from the RENI project [24]. Figures 3–5 depict the experimental skin-friction line patterns, PIV data-extracted vortex core trajectories, and CFD-predicted streamlines around the RENI model, respectively, for an angle of attack $\alpha = 12$ deg and a freestream velocity $V_\infty = 40$ m/s, at sea-level International Standard Atmosphere (ISA). On the inner side of the nacelle, both skin-friction lines (Fig. 3) and light blue and green streamlines (Fig. 5) exhibited a strong sideslip close to the pylon, whereas on the outer side of the nacelle, the flow, partly represented by the yellow streamlines, drove along the pylon with a weak sideslip angle. This close-to-pylon/nacelle junction flow topology, also reported

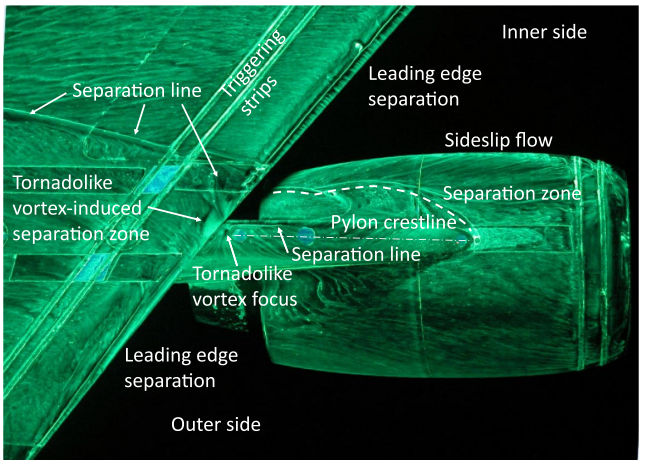

Fig. 3 Viscous-coating-based skin friction line patterns on the RENI model surface [24].

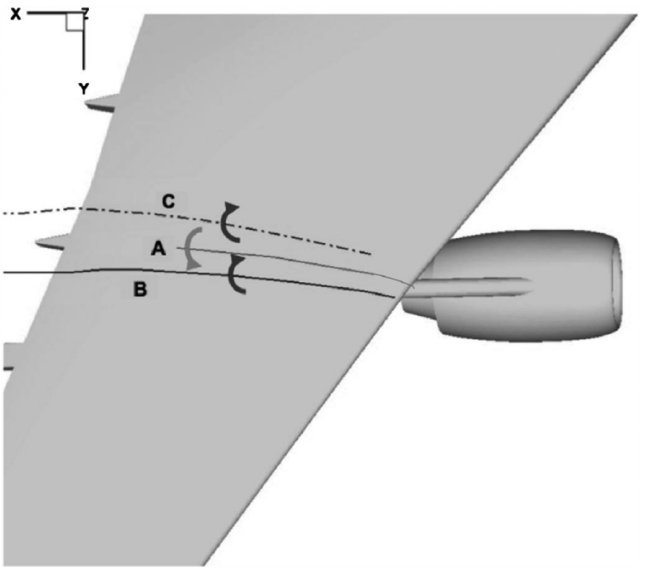

Fig. 4 Vortex trajectories (PIV measurements) along the suction side of the RENI model [24].

by Yokokawa et al. [19], was promoted by both the nacelle design and the swept wing that induced a compression zone on the inner side of the nacelle cowling. The latter partially blocked the flow and promoted a separation zone, clearly identified in Fig. 3 and delimited by a white dotted line, at the junction between the inner side of the nacelle and the pylon. Consequently, the flow moved toward the pylon with a sideslip angle of approximately 30 deg. It resulted in a shear flowfield on the pylon crest line. Therefore, a tornadolike vortex, noted A in Fig. 4 and characterized by a low axial velocity in its core, initiated at the intersection between the wing leading edge and the pylon crest line. This vortex is clearly represented by the dark blue streamline rolling up (Fig. 5) and by the presence of a focus also visible experimentally through oil-flow visualization (Fig. 3). It was then advected very close to the upper-wing wall and interacted with the boundary layer. This close-to-wall interaction was revealed by the separation line on the skin-friction line patterns observed on the suction side of the wing (Fig. 3). This vortex promoted a local flow separation at the leading edge of the wing (Fig. 3) and was responsible for the inception of a second vortex of opposite vorticity sign (noted B). This vortex traveled at a larger distance from the wall than vortex A, and this did not significantly affect the skin-friction line patterns. The third identified vortex (noted C) initiated from the previously mentioned separation zone located on the inner side of the nacelle, at the junction with the pylon.

To recover a similar flow topology on the simplified model, the nacelle obstruction and the swept wing effect have been replaced by a sideslip-angle effect on the geometry. Two angle of attack

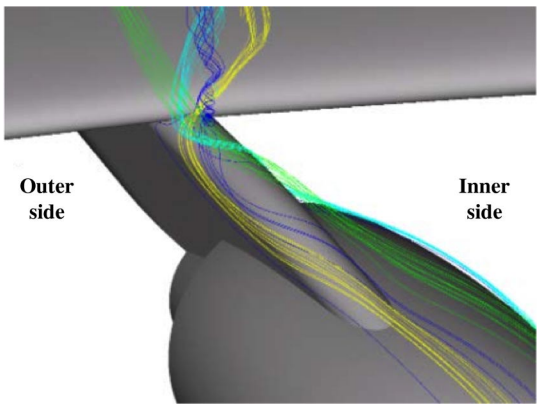

Fig. 5 CFD-predicted streamlines around the RENI model [24].

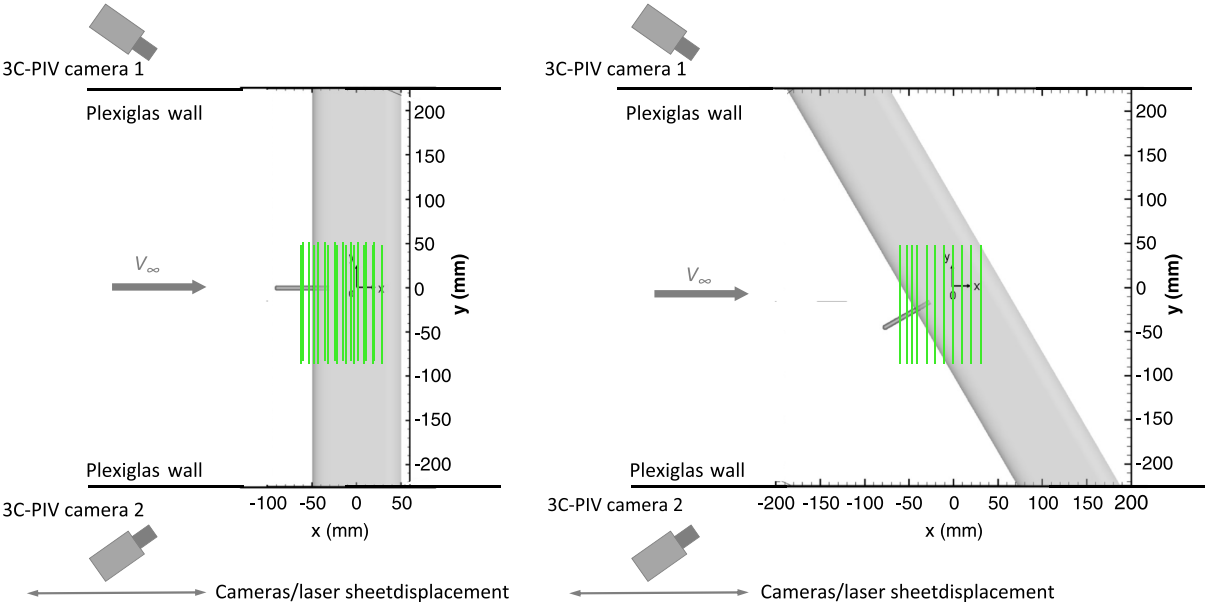

Fig. 6 Schematics of the simplified model in the WT, for conf1 (left) and conf2 (right).

α and sideslip angle β configurations ($\alpha = 8$ deg $/\beta = 0$ deg) and ($\alpha = 8$ deg $/\beta = 30$ deg), hereafter denoted conf1 and conf2, respectively, have been investigated by means of URANS computations, oil-flow visualizations, and 3C-PIV measurements. Figure 6 provides the schemes of the simplified model in the WT for conf1 and conf2, respectively. The green lines on the figures depict the transverse PIV measurement planes.

III. Experimental Apparatus

A. WT Setup and Test Model

Experiments were performed in a low-speed WT at ISAE, Toulouse [36–38]. It is a closed-loop, continuous flow tunnel with a freestream velocity V_∞ ranging from 5 to 30 m/s. The turbulence intensity in the working test section was tuned to 1.5%. At $V_\infty = 30$ m/s, the freestream velocity uncertainty was below 0.3 m/s. The test section was a (0.45×0.45) m^2 cross section, 0.7 m long with four transparent 10-mm-thick Plexiglas walls. The model support system consisted of two wedges embedded in the left and right Plexiglas walls (Fig. 7). Several interchangeable wedge sets allowed the angle of attack α and the sideslip angle β of the model to be adjusted. The rotation center of the model was located at the center of the test section, at midchord and at midspan of the wing. To avoid wingtip vortices able to disturb the flowfield around the cylinder/wing intersection, the wingspan was extended to the sidewalls.

B. Experimental Methods

To analyze the vortical flow past the simplified model, two experimental methods were used. First, oil-flow visualizations were performed with a mixture composed of oleic acid, white spirit, and a phosphorescent tracer. This technique reveals the pattern of the skin-friction lines. Second, 3C-PIV measurements were achieved to better investigate the flowfield around the cylinder/wing junction and the upper wing, and to provide an exhaustive database for CFD validation. The 3C-PIV system was a Hub-type Dantec Dynamics system. It was composed of a laser illumination source; two highly sensitive digital imaging devices; and dedicated hardware and software for laser/camera synchronization, data acquisition, and analysis. The illumination source was a frequency-doubled double-cavity Nd:YAG laser operating at a wavelength of 532 nm (200 mJ/7 ns per pulse) and a tunable pulse rate up to 15 Hz. The overlapped core beams were expanded into a 17 deg diverging light sheet using focusable sheet-forming optics. At the measurement station, the laser sheet thickness was adjusted to approximately 2 mm. Recording of particle image pairs was accomplished via two 8-bit double-frame charge-coupled device cameras with a sensor resolution of 4000×2672 pixel^2. The cameras were equipped with two Nikon 105 mm $f/2.8D$ lenses. A pair of special mounts that allow for the rotation of the camera body with respect to the lens was used so as to meet the Scheimpflug principle. The flow seeding, composed of water-based spherical particles, was produced by a ZR33 fog generator located in the WT, aft the fan. The seeding particle size was determined with a Spraytec phase Doppler anemometry system. The mean particle diameter was around 1.6 μm.

To reduce reflections of the laser sheet on the model, a black screen layer was applied on the surface. This screen layer was covered with a rhodamine 6G organic coat (Fig. 7). This coating fluoresces orange when excited with a 532-nm-wavelength light. A narrowband 3-nm-width interference filter, centered on 532 nm, was fixed in front of each camera lens. As such, reflections induced by the impact of the laser sheet on the model were strongly mitigated and the near-wall flowfield could be well captured on the images.

The laser was set up above the test section and cameras were positioned on both sides of the test section. Both laser and cameras were fixed together on a micrometric displacement table controlled by the PIV software. Figure 7 depicts the two cameras located out of the WT test section [here, for conf1 ($\alpha = 8$ deg $/\beta = 0$ deg)]. Processing of the images to derive instantaneous velocity vector maps

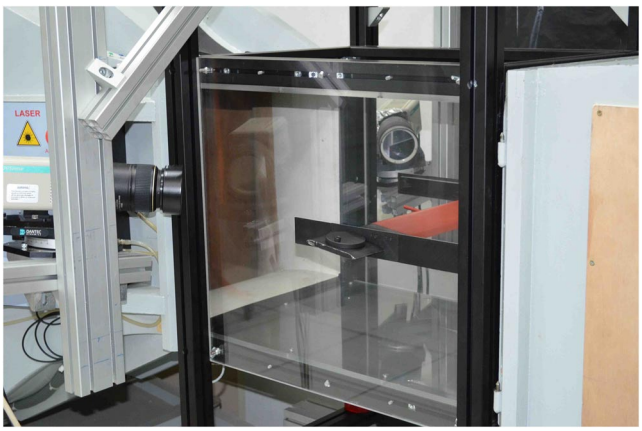

Fig. 7 Simplified model setup, coated with rhodamine 6G, in the test section (conf1).

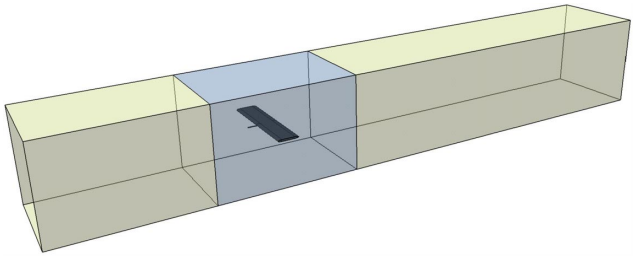

Fig. 8 Computational domain with the simplified model positioned following conf1.

was done using an adaptive PIV algorithm. The final interrogation window size was 32×32 pixel^2, with 50% overlap. This yields raw vector fields of up to 170×115 vectors for transverse measurement plane dimensions of approximately 130×90 mm.

Ten and eleven transverse measurement planes were acquired for conf1 and conf2, respectively, spanning from $x/c = -0.6$ to $x/c = 0.4$, in which x stands for the streamwise direction. Their locations are depicted in Fig. 6. For each measurement plane, 300 pairs of images were collected per camera to evaluate the statistical characteristics of the flow. Each pair constituted of two 5 μs time-interval separated images. Statistical calculations included mean velocities along the x, y, and z directions; standard deviations; covariance; and correlation coefficients.

IV. Computational Method

The numerical model was generated in accordance with the WT model. Figure 8 illustrates the simplified geometry in the overall computational domain for conf1. Its length is $10c$ upstream and $20c$ downstream of the center of the model. The actual WT test-section cross dimensions imposed both height and width of the computational domain. The latter are equal to $4.5c$. For mesh simplification consideration, the WT diffuser and collector were not modeled.

A chimera mesh approach was applied for this study [36–38]. The mesh, illustrated in Fig. 9a, is composed of three overlapping structured blocks: a background grid (shaded in red in Fig. 9), a C-grid topology around the wing (shaded in green), and a refined grid (shaded in blue) around the cylinder/wing junction where the vortices are expected to initiate. The different steps of mesh transformation associated with the chimera approach were detailed by Eliasson et al. [21]. This chimera method allows changing both the angle of attack α and sideslip angle β of the model by rotating both refined and wing boxes relative to the background grid, and therefore, to remain at isomesh conditions around the model. A specific mesh effort was devoted at the cylinder/wing junction by using a C-90-grid topology to keep convenient cell orthogonality (Fig. 9b). A grid optimization strategy, based on the mesh density effect in the refined grid and relying on both the evolution of the drag and lift coefficients of conf1 and on the global flowfield topology in terms of streamwise vorticity isocontours, was performed (see [36] for a comprehensive description of the mesh convergence study). It permitted to fix the size of the mesh to 19×10^6 computational cells as the most appropriate for the following study. On the model walls, the size of the cells was fixed, such as to ensure $y+$ values below 1.

The zone of interest, located in the vicinity and in the wake of the pylon/wing junction, was far enough from the boundaries of the domain. Indeed, no viscous effects were considered on the lateral walls of the computational domain where a slip condition was applied. It should be mentioned that a preliminary study, detailed in [36], has been conducted to investigate the influence of the boundary conditions and the size of the computational domain—extended computational domain with far-field conditions and slip or no-slip conditions on the walls of the simulated test section—on the flowfield in the zone of interest of the model. The comparison, based on both the aeroforces exerting on the model and on the local pressure distribution at different sections along the span of the wing, did not reveal any noticeable effect. An adiabatic no-slip boundary condition was applied on the model. Pressure far-field conditions were imposed at the inlet and outlet of the computational domain.

All computations were conducted with the multiblock structured elsA solver [39], which solves the compressible 3-D URANS equations with a cell-centered finite volume formulation. A low-speed preconditioning algorithm and a V-cycle multigrid method were used to improve and accelerate the convergence, respectively. Spatial discretization was carried out with the centered second-order Jameson scheme. From the experience gained in the RENI project, the two-equation $k - \omega$ turbulence model from Menter [40] with shear-stress transport (SST) correction was applied.

URANS computations were initialized by a RANS solution obtained after 5000 iterations. Then, a dual time-stepping approach was applied with a time step $\mathrm{dt} = 10^{-5}$ s, based on a time-step convergence study fully detailed in [36]. The unsteady computations were then performed on 10,000 time steps, corresponding to 30 time units, based on the chord c and on the freestream velocity V_∞. The presented results were averaged on the basis of the last 2000 time steps (i.e., 20 ms), ensuring both the statistical convergence of the averaging and that the transitory step was past.

Finally, the far-field flow conditions (pressure, temperature, Mach number, and turbulence intensity) were fixed in accordance with the experimental conditions. Fully turbulent flow conditions were assumed.

V. Results and Discussion

Following the description of the method used to characterize the vortex dynamics, this section presents both experimental and numerical results for conf1 ($\alpha = 8$ deg $/\beta = 0$ deg) and conf2 ($\alpha = 8$ deg $/\beta = 30$ deg). The freestream velocity was fixed to $V_\infty = 30$ m/s. The corresponding Reynolds number Re_c, based on the chord c of the model and on V_∞ for an airstream at ISA conditions, equals 2×10^5.

A. Vortex Tracking Method

To gain a better knowledge of the flow dynamics promoted by the power-plant installation/wing interaction, it is crucial to decipher the vortical activity initiated by the pylon/wing junction. To this avail and on the basis of both PIV and CFD flowfield databases, the vortex structures that developed past the model were identified using the λ_2 criterion [41]. The latter were then analyzed via a vortex tracking algorithm, described in more detail in [26] and summarized as follows.

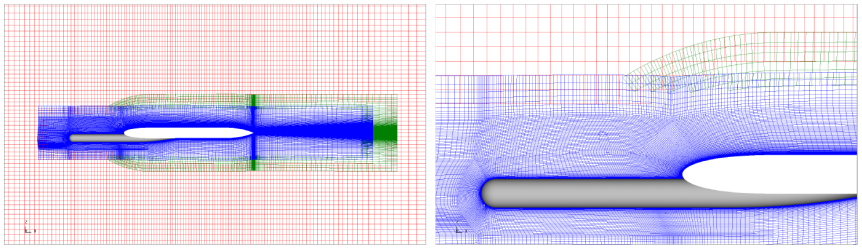

a) **b)**

Fig. 9 a) Overlapping grids, b) grid topology nearby the cylinder/wing junction.

From both transverse-to-streamwise-flow 3C-PIV measurement planes and corresponding CFD planes, at a given streamwise position x, the vortex cores are defined as connected regions Σ of the negative λ_2 criterion. It is important to mention that λ_2 can be accurately computed on the basis of *two-dimensional* (2-D) flowfields (imposed by the PIV measurement planes), because it has been verified that the x derivatives $\partial/\partial x$ of the velocity components are order-of-magnitude lower than the y and z derivatives $\partial/\partial y$ and $\partial/\partial z$. The vortex kinematic parameters are then determined as follows:

$$\Gamma = \iint_{\Sigma} \omega_x \, dy \, dz \tag{1}$$

in which ω_x refers to the streamwise vorticity distribution in the core Σ, and Γ is the vortex circulation (hereafter denoted intensity).

The positions (y_c and z_c) of the vortex centroid are then given by

$$y_c = \frac{1}{\Gamma} \iint_{\Sigma} y\omega_x \, dy \, dz \tag{2a}$$

$$z_c = \frac{1}{\Gamma} \iint_{\Sigma} z\omega_x \, dy \, dz \tag{2b}$$

The vortex core radius R can be defined based on polar moments of vorticity [42]:

$$R = \left[\frac{1}{2} \iint_{\Sigma} ((y - y_c)^2 + (z - z_c)^2)\omega_x \, dy \, dz/\Gamma \right]^{1/2} \tag{3}$$

B. Conf1 ($\alpha = 8$ deg /$\beta = 0$ deg)

The main objective of conf1 was to provide a database for the validation of the numerical approach, on a partially known and documented vortex dynamics induced by a hemispheric cylinder at a moderate incidence and interacting with the wing boundary layer. The flowfield around a hemispheric cylinder facing a 10 m/s freestream for a range of incidence from 0 to 90 deg was experimentally studied by Hoang [43]. Figure 10, extracted from his work, is provided to assist the reader in the understanding. From an incidence $\alpha = 10$ deg, a strong crossflow developed on both sides of the cylinder and promoted the separation of the boundary layer. The latter rolled up into a pair of leeward vortices, clearly identified by a pair of separation lines on the cylinder surface. Because of the hemispherical nose design, two smaller horn vortices initiated close downstream the nose. The skin-friction patterns denote a closed-type separation in this region.

Figure 11 depicts a close-up view of skin-friction line patterns on the cylinder (Fig. 11a) and cross planes of normalized streamwise vorticity isocontours along the chord of the simplified model (Fig. 11b), extracted from the computational results. As expected and described in [43], two main counter-rotating leeward vortices rolled up on both sides of the cylinder plane of symmetry. They are consecutively advected on the upper wing. In addition, two lower-amplitude vorticity pockets were identified on the two first cross planes, at $x/c = -0.8$ and $x/c = -0.7$, close downstream the hemispherical nose. The latter are associated with the separation area visible on the skin-friction lines in Fig. 11a. They correspond to the horn vortices. Finally, the overall flow topology past the cylinder at a moderate incidence was well predicted by the computations in comparison with the description of [43].

Each vortex was characterized in terms of a vortex core associated with a streamwise vorticity pocket. As depicted in Fig. 11b, the $1N$ and $1P$ vortices are associated with negative and positive streamwise vorticity pockets, respectively. In their rolling-up process, induced by a strong upward/crossflow on each cylinder side, the boundary layer separated along two separation lines (Fig. 11a). These separation lines converged toward the cylinder crest, near the intersection with the wing leading edge. Then, the two vortices separated and were advected along the upper wing. As they were advected along the cylinder, they interacted with the boundary layer and induced, below them, a region of opposite signs of vorticity, leading to the occurrence of two weaker counter-rotating vortices, also denoted secondary vortices. In the first half-chord of the wing, the latter, visible in the close view provided in Fig. 12, were pushed out of the $1N$ and $1P$ vortices by deforming them. After the dissipation of the secondary vortices at $x/c \approx -0.25$, the shape of the streamwise vorticity pockets associated with the $1N$ and $1P$ vortices flattened to an elliptic shape. By interacting with the wing boundary layer, the $1P$ and $1N$ vortices induced regions of opposite vorticity signs below them. However, these vorticity pockets were not strong enough to trigger, in their upwash region, a local separation able to produce a secondary vortex of opposite vorticity. This kind of vortex/boundary-layer interaction was reported by Pauley and Eaton [44] in their experimental results of the interaction of a longitudinal vortex pair with a turbulent boundary layer without a pressure gradient.

To gain a better knowledge of the interaction between the vortices and the boundary layer, a top view of the vortex path, determined from the vortex tracking algorithm applied to the PIV measurements, is superimposed (blue and red dotted lines with circle markers) with oil-flow visualizations in Fig. 13a. Figure 13b provides a comparison with the skin-friction line patterns obtained from the CFD results.

The experimentally determined $1N$ and $1P$ vortex core paths are colored in blue and red, respectively. The scatter size is a function of the vortex core radius. It is provided for illustration convenience. First, Fig. 13 reveals two separation areas: at the leading edge and at the trailing edge of the wing. The leading-edge curvature and the thin

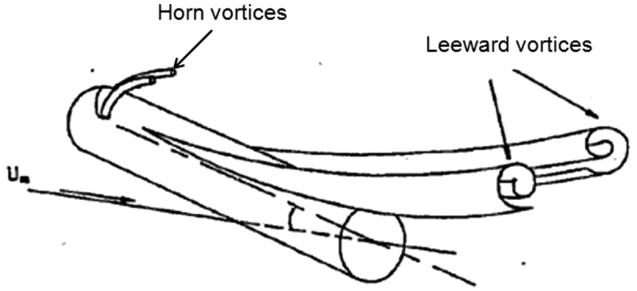

Fig. 10 Schematic of the vortex structures past a hemispheric cylinder at moderate incidence [43].

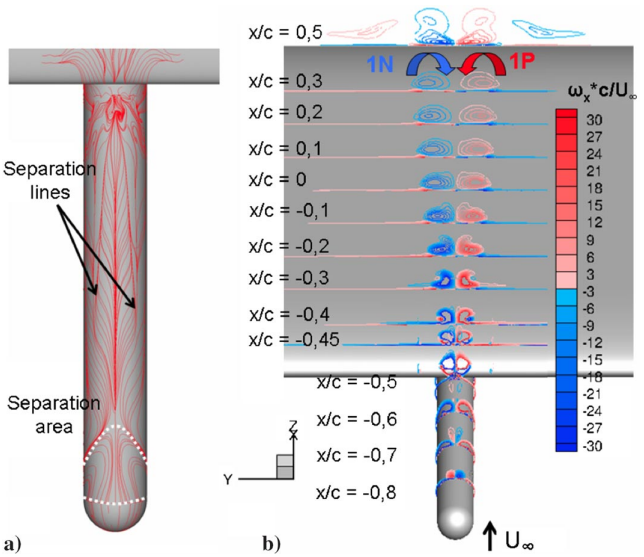

Fig. 11 a) Skin-friction line patterns, b) isocontours of normalized streamwise vorticity (conf1).

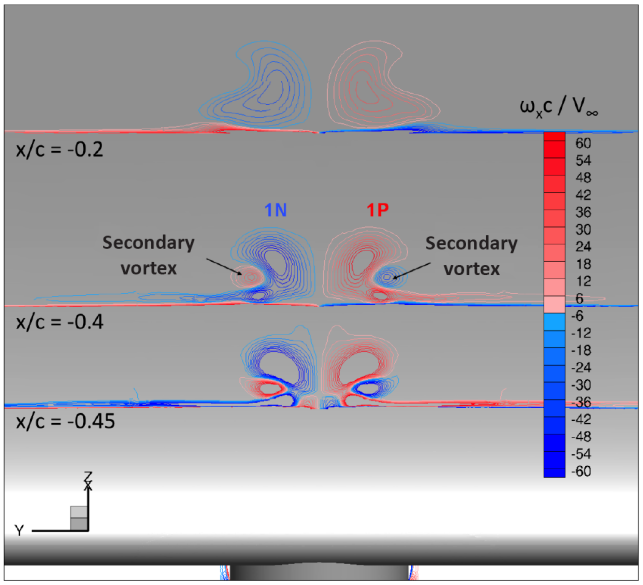

Fig. 12 Close view of $\omega_x c/V_\infty$ cross planes (conf1), revealing secondary vortices occurrence.

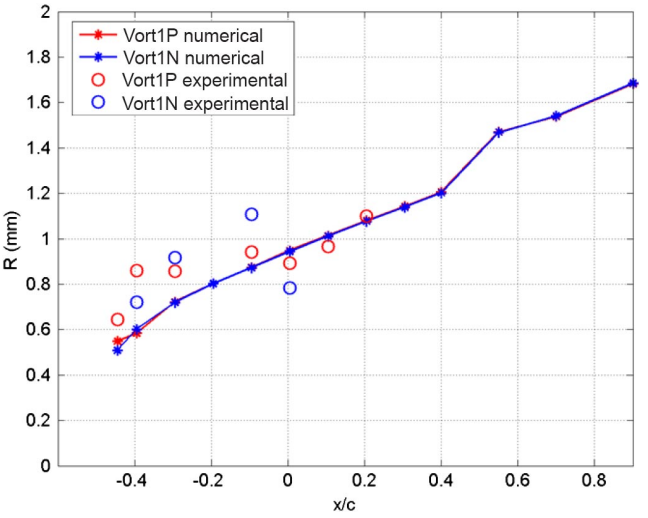

Fig. 14 Streamwise evolution of 1*N* (blue) and 1*P* (red) vortex core radius *R*.

relative thickness of the wing profile, associated to low-speed conditions, induced a laminar separation bubble at the leading edge. With the imposed ambient turbulence in the WT section, this resulted in a natural laminar-to-turbulent boundary-layer transition, ensuring turbulent conditions on the model. The trailing-edge separation was triggered by the adverse pressure gradient imposed by the aft model curvature. The two separation lines revealed the interaction between the upper-wing boundary layer and the 1*N* and 1*P* vortices. According to a common downflow vortex-pair effect, their trajectories were located slightly inward the separation lines, which are evidenced by the mixture buildup in the upwash region of the vortices. This resulted in a progressive lateral divergence of both 1*N* and 1*P* vortices. The computational results depicted in Fig. 13b show that the size of the trailing-edge separation is slightly underestimated in comparison with the experimental results. Despite this, a good agreement was observed between the computed skin-friction line pattern and the WT oil-flow visualization.

The evolution in the streamwise direction of the vortex core radius R and the normalized intensity $\Gamma/(V_\infty c)$ are plotted in Figs. 14 and 15, respectively, for both the 1*N* and 1*P* vortices. The 3C-PIV measurements efficiently captured these two very small vortices, despite the fact that they were partially embedded in the boundary layer. Because of their too small sizes, the secondary vortices described in Figs. 11 and 12 were not captured experimentally. It should be recalled that the final interrogation windows were 32×32 pixel^2 with a 50% overlap, corresponding to a resolution about 0.6×0.35 mm^2. As such, the size of the vortical structures detected up to the cross section $x/c = -0.2$ is close to the limit size achievable with this measurement technique.

The symmetry of this vortical flowfield, clearly observed in Figs. 11–13 (relative to the plane of symmetry of the cylinder), is confirmed in Figs. 14 and 15 in terms of both similar 1*N* and 1*P* vortex core radius and amplitude of their normalized intensity. The streamwise evolution of experimental and computational vortex

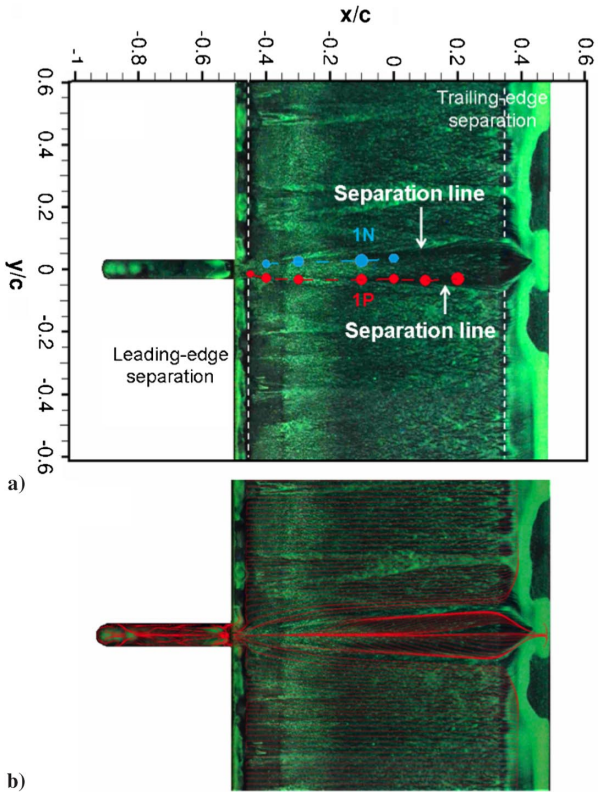

Fig. 13 a) Experimental and b) computational skin-friction line pattern (red lines) conf1.

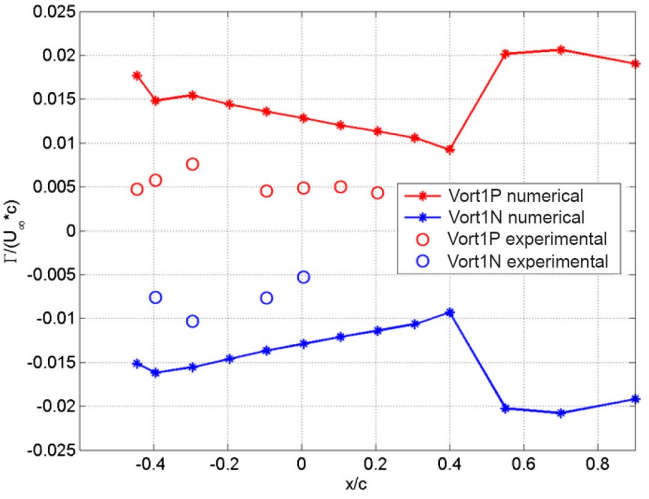

Fig. 15 Streamwise evolution of 1*N* (blue) and 1*P* (red) normalized vortex core intensity $\Gamma/(V_\infty c)$.

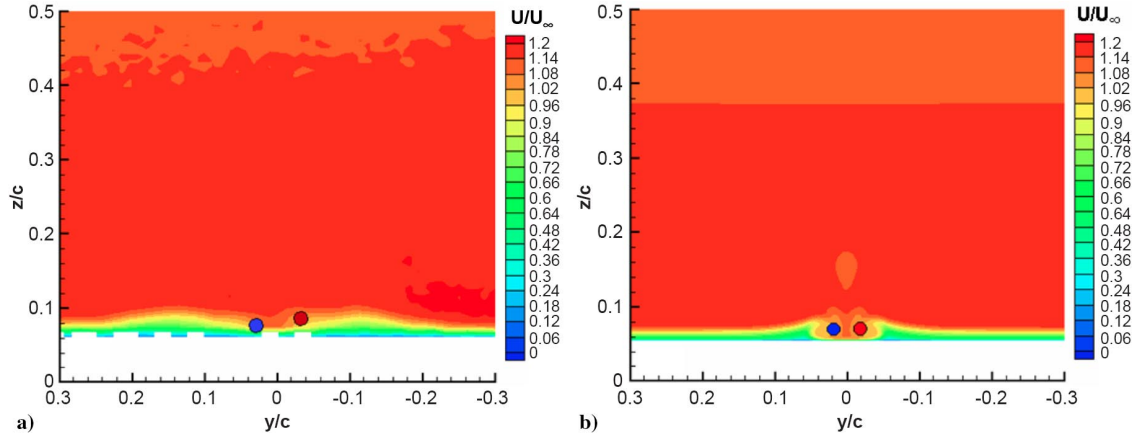

Fig. 16 a) Experimental, b) CFD normalized streamwise velocity isocontours and vortex cores (markers) at $x/c = -0.1$.

core radii follows a similar trend, characterized by a progressive increase. Between cross sections $x/c = -0.3$ and $x/c = 0.4$, on the flat part of the model, the two vortex cores grew linearly, whereas their circulations continuously and linearly decreased.

As the vortices left the wall, both vortex core radii and intensities suddenly increased. Then, in the wake of the wing, the vortices grew and weakened more slowly than on the wing wall due to an ambient turbulence lower than the one experienced in the upper-wing boundary layer. CFD-predicted vortices are more intense than the actual experimentally observed ones. The associated reasons are investigated here. Near the leading edge, between cross sections $x/c = -0.55$ and $x/c = -0.35$, the wing curvature induced a positive pressure gradient. Consequently, the $1N$ and $1P$ vortex cores were stretched and their intensities increased. Lastly, from the beginning of the flat part of the wing ($x/c = -0.3$), the vortex circulation tended to decrease under the diffusive effects induced by the turbulent boundary layer and skin-friction influence. The interaction between the $1N/1P$ vortex pair and the boundary layer is illustrated in Fig. 16 for cross section $x/c = -0.1$. The $1N$ and $1P$ vortex cores are slightly more spaced (less than 1 mm) in the PIV measurement plane than in the CFD one, and their vertical location slightly differs. Nonetheless, in both cases, the overall impact of this vortex pair on the boundary layer was similarly observed. Indeed, in the upwash region of the vortices, the boundary layer was thickened whereas conversely thinned in the downwash region, between the two vortices. In the experimental case, the boundary layer seemed to be more sensitive to separation, with a more pronounced lateral impact of the vortices on the boundary layer than in computations. Indeed, the separation bubble at the leading edge was slightly different experimentally. Although its streamwise extent is limited in comparison with the numerical one, it is probably thicker in the normal-to-wall direction, promoting a thicker boundary layer, less robust to the pressure gradient imposed by the vortices and the wing in incidence. This was confirmed by the computation of the boundary-layer shape factor H [36]. The CFD- and WT-based shape factors were roughly equal to 1.7 and 1.5, respectively in regions out of the zone of interaction of the cylinder-induced vortices with the boundary layer. This value increased up to 2.05 in the vortex-induced upwash zones, then decreased down to 1.3 and 1.5 for the CFD results and WT test (WTT) measurements, respectively, in the downwash zone located between the two vortices initially generated by the cylinder/wing junction. These values confirmed the robustness of the boundary layer to separation.

C. Conf2 ($\alpha = 8$ deg $/\beta = 30$ deg)

By positioning the model in sideslip configuration, the flowfield was made much more complex. Figure 17 depicts the cross planes of normalized streamwise vorticity isocontours along the chord of the model. Figure 18 provides a closer view of the latter at the cylinder/wing junction and in the first half of the upper wing, between $x/c = -0.5$ and $x/c = -0.2$.

Two leeward vortices, noted $1N$ and $1P$, respectively (N for negative; P for positive vorticity sign) initially rolled up along the cylinder. They were consecutively advected along the wing. The $1P$ vortex, initially located below the $1N$ vortex, impacted the wing leading edge and was split into two longitudinal vortices. The latter separated at the leading edge and were advected along the upper and lower wings, respectively. When the $1N$ vortex separated from the cylinder near the wing junction, part of its associated vorticity pocket tended to reattach on the surface. Nevertheless, due to the upper-wing suction, this negative vorticity pocket rolled up to form a vortex, noted $2N$ (see Fig. 18 for a close view). On the left-hand side of this vortex, another negative streamwise vorticity pocket associated with a new vortex was identified. The latter was a small tornadolike vortex, initiated on the cylinder surface and that was advected very close to the upper-wing wall. This vortex and the $2N$ vortex rapidly merged, around $x/c \approx -0.3$, while traveling downstream along the surface of the model. In the upstream part of the wing, they interacted with the upper-wing boundary layer, promoting a counter-rotating vortex, noted $2P$. The path of this vortical structure is identified in Fig. 17 by an orange dashed line. Finally, on the right-hand side of the $1N$ vortex and under its influence, the boundary layer separated. This promoted the inception of a last vortex, noted $3P$. The latter was only detected in CFD, and its trajectory is associated with the red dashed line in Fig. 17.

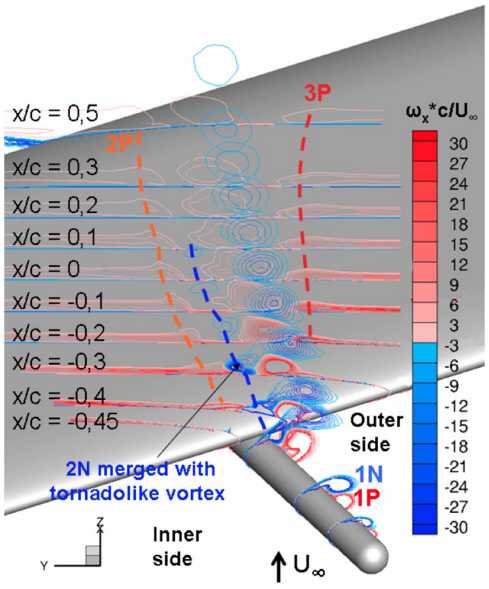

Fig. 17 Cross planes of isocontours of normalized streamwise vorticity at various positions x/c (conf2).

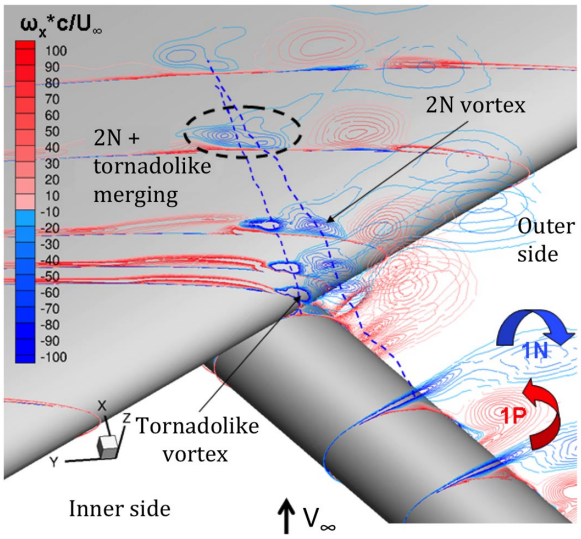

Fig. 18 Close view of normalized streamwise vorticity $\omega_x c/V_\infty$ isocontours.

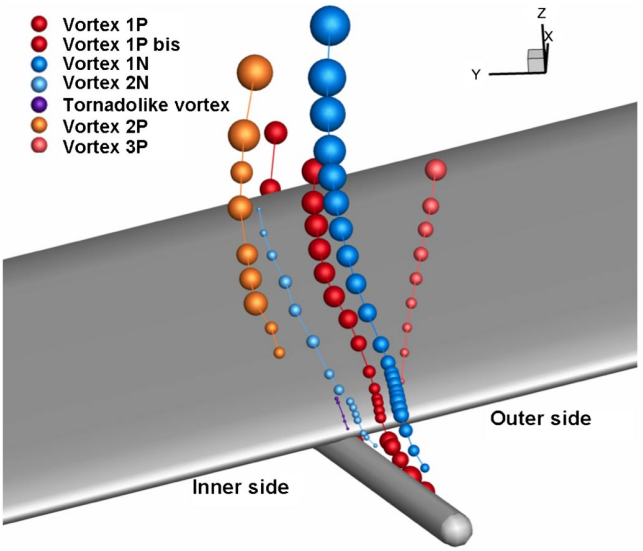

Fig. 20 Trajectories of the vortices on the model (sphere diameter proportional to vortex core radius).

To have a better understanding of the tornadolike vortex occurrence and of its impact on the boundary layer, the flowfield nearby the cylinder/wing junction is depicted in Fig. 19. On the inner side of the model in sideslip configuration, streamlines came above the cylinder, whereas on the outer side, they moved along the cylinder up to a stagnation point. This flowfield was then influenced by both wing suction and shear. As a consequence, streamlines rolled up on the cylinder crest around a focus, characterized by a local drop of pressure coefficient, clearly visible in Fig. 19a. The total pressure was low in the core of this small tornadolike vortex (Fig. 19b). The latter interacted with the leading-edge boundary layer, still disturbed by the presence of the cylinder. Thus, a flat separation bubble was triggered near its upwash region (blue flat region encircled by a dashed ellipsis in Fig. 19b). It was confirmed by the values of the shape factor, which increased up to 2.3 in this zone, and then decreased down to 2.1 when moving away in the spanwise direction [36]. As mentioned previously, this resulted in a lack of momentum and the progressive occurrence of a secondary vortex identified as the $2P$ vortex (Fig. 17). The overall CFD-predicted vortex dynamics described previously is illustrated in Fig. 20. It should be mentioned that, due to the tiny size of the tornadolike vortex and to its proximity to the wall, and considering the cross-plane orientation imposed by the PIV measurement planes, this vortex was captured neither in PIV measurement planes nor in most of the CFD planes.

Oil-flow visualizations, depicted in Fig. 21, revealed two separation areas at both the leading edge and trailing edge of the wing. Because of the crossflow induced by the model sideslip angle $\beta = 30$ deg, they are narrower than the ones observed for conf1, except for one small leading-edge region near the cylinder. On the inner side of the model, the presence of the cylinder in incidence ($\alpha = 8$ deg) induced a blockage effect responsible for a local flow separation, and thus, an oil-based mixture accumulation. By zooming on the cylinder/wing junction, a small separation bubble was observed. It is identified in Fig. 21b by a white circle and was located on the left-hand side of the separation line. This region should be connected with the flat separation bubble described previously. As illustrated in Fig. 21, three vortices were identified through 3C-PIV measurements. The $1N$, $1P$, and $2P$ vortex paths are colored in blue, red, and orange, respectively. One separation line was clearly observed, which extends from the wing leading edge to the trailing edge. Close to the leading edge, this line was collinear to the cylinder (Fig. 21b) and did not follow any of the PIV-identified vortex trajectories. Based on the previously mentioned results, this separation line was most probably generated by both the tornadolike vortex and the $2N$ vortex. At $x/c = -0.2$, the separation line shifted when the $1P$ vortex dissipated, and then followed the flowfield direction between the $1N$ and $2P$ vortices. Downstream the PIV measurement plane located at $x/c = 0.3$, a zone of accumulation of the oil-based viscous coating was observed. It was probably induced by a boundary-layer separation, initiated by the interaction of both the $2P$ and $1N$ vortices with the boundary layer.

The streamwise evolution of parameters R and $\Gamma/(V_\infty c)$ and of the vertical position z/c of the vortex cores is depicted in Figs. 22–24, both for experimental and computational data. Figures 22–24 reveal an overall good agreement between the experiments and the computations, especially for the $1N$ vortex, which evolved slightly further away from the wall than the other vortices. In Fig. 22, the only noticeable difference was observed for the $2P$ vortex that was

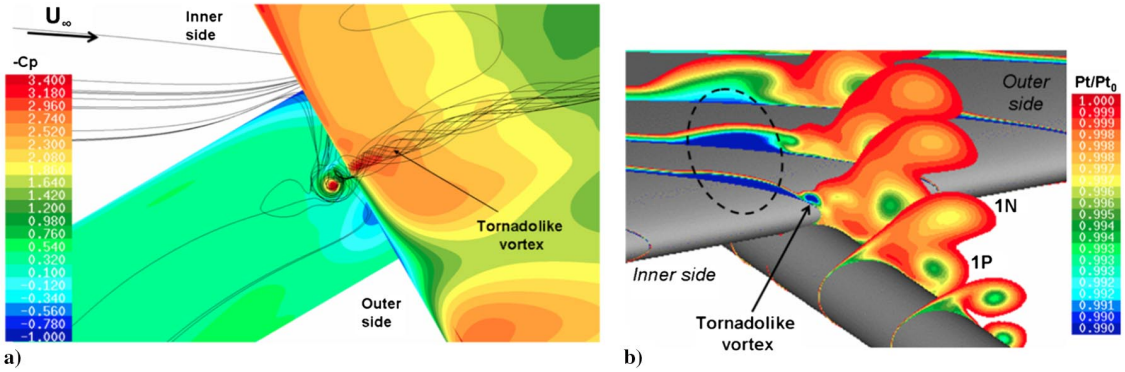

Fig. 19 a) Streamlines and $(-Cp)$ distribution; b) cross planes of normalized total pressure distribution P_t/P_{t_0}.

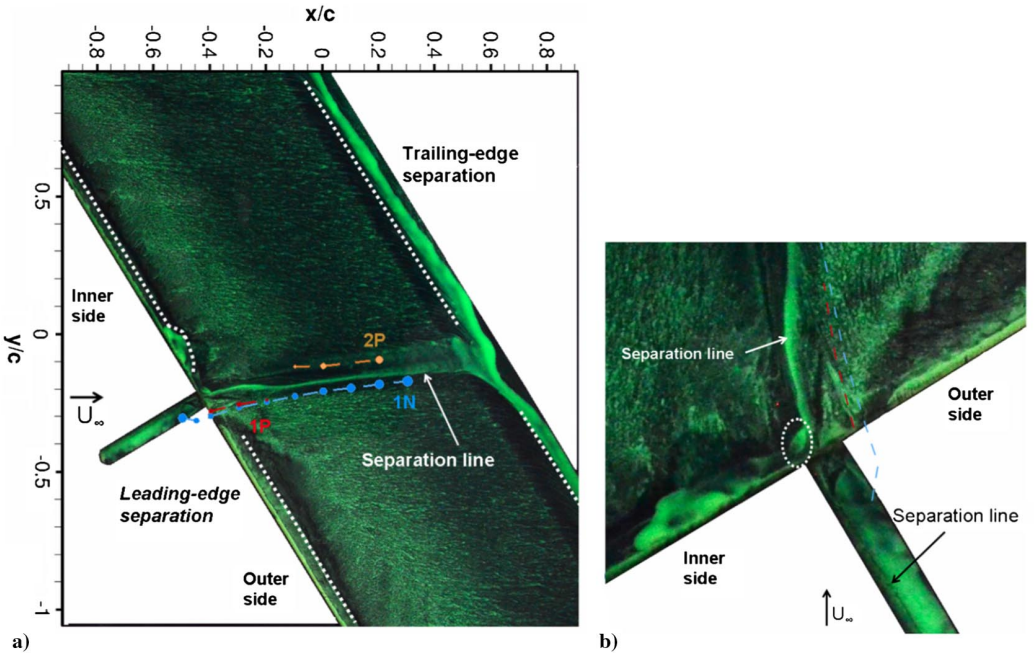

Fig. 21 a) Experimental skin-friction line pattern, b) detailed view at the cylinder/wing junction.

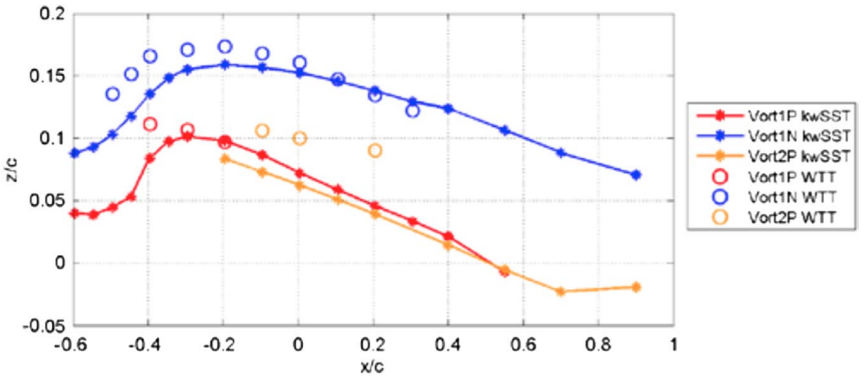

Fig. 22 Streamwise evolution of the vortex core vertical position z/c.

advected closer to the wall in the CFD in comparison with the experimental results. Subsequently, the analysis of these vortex dynamics will essentially be performed on the basis of PIV measurements. Even if the $1N$ vortex evolved further away from the wing than the other vortices, it remained close to the wall and followed the upper-wing wall curvature. The other vortices obeyed an identical behavior. Between cross planes $x/c = -0.4$ and $x/c = 0.4$, all the vortex cores grew in size (Fig. 23). One can notice that the streamwise evolution of the $1N$ vortex core radius follows a linear trend. Regarding the evolution of both $2P$ vortex core radius and normalized intensity, this vortex seems to be promoted not only by its interaction with the $1N$ vortex, but also by the positive streamwise vorticity of the boundary layer induced by the crossflow on the upper wing (Fig. 17). As a consequence, its radius drastically grew and its intensity slightly increased when it traveled downstream, as illustrated in Fig. 24. However, it remained relatively weak. Initially, the $1N$ vortex circulation dropped by half when it separated from the cylinder (see Fig. 24; experimental curve, also referred to with the acronym

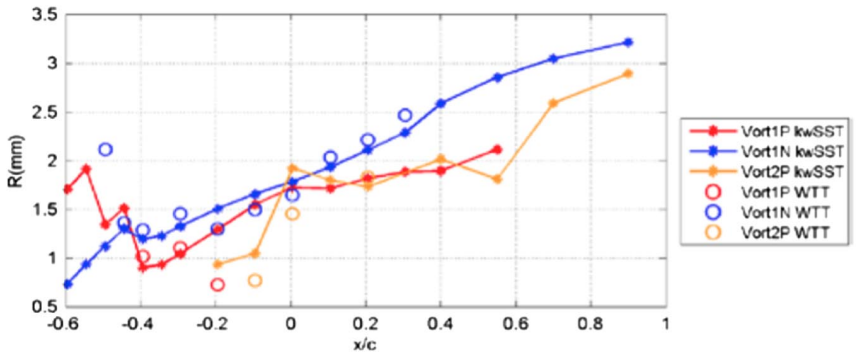

Fig. 23 Streamwise evolution of the vortex core radius R.

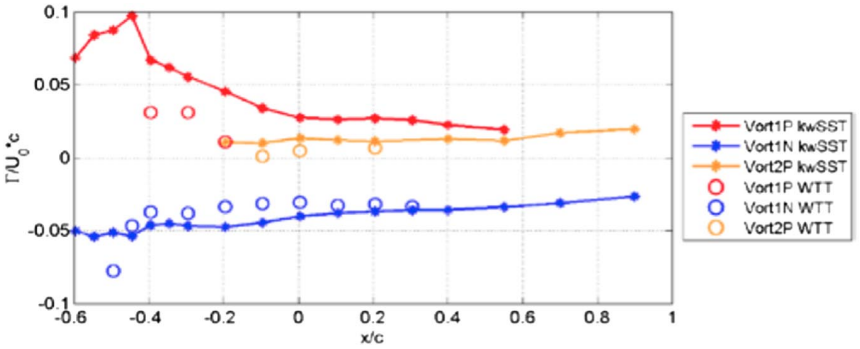

Fig. 24 Streamwise evolution of the normalized vortex core intensity $\Gamma/(V_\infty c)$.

WTT). Then, its intensity progressively decayed until it reached a plateau, from $x/c = 0$. On the opposite, the $1P$ vortex, compressed between the $1N$ vortex and the wing, was rapidly dissipated, as revealed by its drop of circulation.

VI. Conclusions

In this study, the flow past a simplified geometry of a wing equipped with a pylon-mounted engine at low-speed/moderate-angle-of-attack flight conditions has been numerically and experimentally investigated, by means of URANS computations, oil-flow visualizations, and 3C-PIV measurements. Two configurations of angle of attack and sideslip angles ($\alpha = 8$ deg $/\beta = 0$ deg) and ($\alpha = 8$ deg $/\beta = 30$ deg) have been investigated. The vortex dynamics thus produced has been described in terms of vortex core position, intensity, and size. First, the configuration ($\alpha = 8$ deg $/\beta = 0$ deg) has been studied to validate the numerical approach, thanks to a comparison with the experimental results and the literature. This configuration was characterized by the separation and the longitudinal rolling up of the cylinder boundary layer into two main counter-rotating vortices distributed on both sides of the cylinder plane of symmetry (P). Then, they were advected along the upper wing. Vortical topology was symmetric relative to the plane (P), both for the vortex trajectories, intensities, and core radii. Superimposed with oil-flow visualizations, the vortex core trajectory clearly corroborated the separation lines located over the wing. Second, the analysis of the configuration ($\alpha = 8$ deg $/\beta = 30$ deg) brought to light a more complex vortex dynamics, close to the one observed for a real aircraft in high-lift flight conditions. This vortex dynamics interacted and disturbed the upper-wing boundary layer. Close to the wing/cylinder junction, the highly sheared flow promoted the occurrence of a tornadolike vortex on the pylon crest. The latter was advected close to the leading edge of the upper wing and locally triggered a boundary-layer separation in its upwash region. This induced a secondary counter-rotating vortex. As for the first configuration, two counter-rotating vortices separated from the cylinder. Because of the sideslip angle, a clockwise principal vortex was advected on the upper wing. A good experimental vs numerical correlation was obtained in terms of vortex core intensity, trajectory, and radius, more particularly for the vortex that evolved further away from the wing than the others. This work is of prime interest to clearly understand the flowfield around the nacelle/pylon/wing junctions. It is a first step in the development of a future efficient flow control strategy.

Acknowledgments

This work was funded within the framework of the CIFRE ISAE/Airbus convention No. 2011-CIF-R71. The experiments and computations have been performed at Institut Supérieur de l'Aéronautique et de l'Espace and Airbus Operation SAS, respectively. The authors would like to thank the ISAE-SUPAERO staff for manufacturing the model and for their technical support, as well as the Airbus Tools and Simulation department staff for their support.

References

[1] Hill, G. A., Kandil, O. A., and Hahn, A. S., "Aerodynamic Investigations of an Advanced Over-the-Wing Nacelle Transport Aircraft Configuration," *Journal of Aircraft*, Vol. 46, No. 1, 2009, pp. 25–35. https://doi.org/10.2514/1.39730

[2] Hurez, A., "Recent Progress on Powerplant/Airframe Integration at Aerospatiale Matra Airbus," *22nd Congress of International Council of the Aeronautical Sciences (ICAS)*, ICAS Paper 2000-2.8.3, 2000.

[3] Wilhelm, R., "Inverse Design Method for Designing Isolated and Wing-Mounted Engine Nacelles," *Journal of Aircraft*, Vol. 39, No. 6, 2002, pp. 989–995. https://doi.org/10.2514/2.3052

[4] Devine, R., Cooper, R. K., Gault, R., Watterson, J. K., and Benard, E., "Comparison of Conventional and Compression Pylon Designs for an Underwing Nacelle," *Journal of Aircraft*, Vol. 46, No. 1, 2009, pp. 325–328. https://doi.org/10.2514/1.34967

[5] Murayama, M., Yokokawa, Y., Yamamoto, K., and Ueda, Y., "Evaluation of Computations and Transition Prediction Method for Aircraft High-Lift Configuration," *Journal of Aircraft*, Vol. 46, No. 5, 2009, pp. 1487–1499. https://doi.org/10.2514/1.34948

[6] Brodersen, O., "Drag Prediction of Engine-Airframe Interference Effects Using Unstructured Navier-Stokes Calculations," *Journal of Aircraft*, Vol. 39, No. 6, 2002, pp. 927–935. https://doi.org/10.2514/2.3037

[7] Langtry, R. B., Kuntz, M., and Menter, F. R., "Drag Prediction of Engine–Airframe Interference Effects with CFX-5," *Journal of Aircraft*, Vol. 42, No. 6, 2005, pp. 1523–1529. https://doi.org/10.2514/1.12728

[8] Wurtzler, K. E., and Morton, S. A., "Accurate Drag Prediction Using Cobalt," *Journal of Aircraft*, Vol. 43, No. 1, 2006, pp. 10–16. https://doi.org/10.2514/1.8589

[9] Malouin, B., Gariépy, M., Trépanier, J.-Y., and Laurendeau, E., "Internal Drag Evaluation for a Through-Flow Nacelle Using a Far-Field Approach," *Journal of Aircraft*, Vol. 52, No. 6, 2015, pp. 1847–1857. https://doi.org/10.2514/1.C033093

[10] Hue, D., Chanzy, Q., and Landier, S., "DPW-6: Drag Analyses and Increments Using Different Geometries of the Common Research Model Airliner," *Journal of Aircraft*, Vol. 55, No. 4, 2017, pp. 1509–1521. https://doi.org/10.2514/1.C034139

[11] Koc, S., Kim, H.-J., and Nakahashi, K., "Aerodynamic Design of Complex Configurations with Junctions," *Journal of Aircraft*, Vol. 43, No. 6, 2006, pp. 1838–1844. https://doi.org/10.2514/1.20723

[12] Zhaoguang, T., Yingchun, C., and Jiangtao, S., "Study of Power Influences to the Wing-Mounted Civil Aircraft Aerodynamic Characteristics," *Journal of Aircraft*, Vol. 51, No. 2, 2014, pp. 629–636. https://doi.org/10.2514/1.C032356

[13] Grönstedt, T., Xisto, C., Sethi, V., Rolt, A., García Rosa, N., Seitz, A., Yakinthos, K., Donnerhack, S., Newton, P., Tantot, N., et al., "Ultra Low Emission Technology Innovations for Mid-Century Aircraft Turbine Engines," *Proceedings of ASME Turbo Expo 2016: Turbine Technical Conference and Exposition GT2016*, ASME Paper GT2016-56123, New York, 2016, p. V003T06A001.

[14] Dietz, G., Mai, H., Schröder, A., Klein, C., Moreaux, N., and Leconte, P., "Unsteady Wing-Pylon-Nacelle Interference in Transonic Flow," *Journal of Aircraft*, Vol. 45, No. 3, 2008, pp. 934–944. https://doi.org/10.2514/1.31363

[15] Schindler, K., Reckzeh, D., Scholz, U., and Grimminger, A., "Aerodynamic Design of High-Lift Devices for Civil Transport Aircraft Using RANS CFD," *28th AIAA Applied Aerodynamics Conference*, AIAA Paper 2010-4946, 2010. https://doi.org/10.2514/6.2010-4946

[16] Metha, R. D., and Lim, T. T., "Flow Visualization Study of a Vortex/Wing Interaction," NASA TM-86656, 1984.

[17] Kato, H., Watanabe, S., Murayama, M., Yokokawa, Y., and Ito, T., "PIV Investigation of Nacelle Chine Effects on High-Lift System Performance," *46th AIAA Aerospace Sciences Meeting and Exhibit*, AIAA Paper 2008-240, 2008. https://doi.org/10.2514/6.2008-240

[18] von Geyr, H., Schade, N., van der Burg, J. W., Eliasson, P., and Esquieu, S., "CFD Prediction of Maximum Lift Effects on Realistic High-Lift Commercial Aircraft Configurations Within the European Project EUROLIFT II," *25th AIAA Applied Aerodynamics Conference*, AIAA Paper 2007-4299, 2007.

[19] Yokokawa, Y., Kanazaki, M., Murayama, M., Kato, H., Ito, T., and Yamamoto, K., "Investigation of the Flow over Nacelle/Pylon and Wing Controlled with a Vortex Generator in High-Lift Configuration," *26th Congress of International Council of the Aeronautical Sciences (ICAS)*, ICAS Paper 2008-3.3.3, 2008.

[20] Yokokawa, Y., Murayama, M., Ito, T., and Yamamoto, K., "Experiment and CFD of a High-Lift Configuration Civil Transport Aircraft Model," *25th AIAA Aerodynamic Measurement Technology and Ground Testing Conference*, AIAA Paper 2006-3452, 2006. https://doi.org/10.2514/6.2006-3452

[21] Eliasson, P., Catalano, P., Le Pape, M. C., Ortmann, J., Pelizzari, E., and Ponsin, J., "Improved CFD Predictions for High-Lift Flows in the European Project EUROLIFT II," *25th AIAA Applied Aerodynamics Conference*, AIAA Paper 2007-4303, 2007. https://doi.org/10.2514/2007-4303

[22] Rudnik, R., and von Geyr, H., "The European High-Lift Project EUROLIFT II—Objectives, Approach and Structure," *25th AIAA Applied Aerodynamics Conference*, AIAA Paper 2007-4296, 2007. https://doi.org/10.2514/6.2007-4296

[23] Kanazaki, M., Yokokawa, Y., Murayama, M., Ito, T., Jeong, S., and Yamamoto, K., "Efficient Design Exploration of Nacelle Chine Installation in Wind Tunnel Testing," *46th AIAA Aerospace Sciences Meeting and Exhibit*, AIAA Paper 2008-155, 2008. https://doi.org/10.2514/6.2008-155

[24] Bury, Y., "Reference Experiments for Nacelle Integration Reports," ISAE-SUPAERO Tech. Rept. WP1 to WP3, 2006–2009.

[25] Rudnik, R., and Germain, E., "Reynolds Number Scaling Effects on the European High-Lift Project Configurations," *Journal of Aircraft*, Vol. 46, No. 4, 2009, pp. 1140–1151. https://doi.org/10.2514/1.36487

[26] Bury, Y., Jardin, T., and Klöckner, A., "Experimental Investigation of the Vortical Activity in the Close Wake of a Simplified Military Transport Aircraft," *Experiments in Fluids*, Vol. 54, No. 5, 2013, pp. 1–15. https://doi.org/10.1007/s00348-013-1524-4

[27] Shizawa, T., and Eaton, J. K., "Turbulence Measurements for a Longitudinal Vortex Interacting with a Three-Dimensional Turbulent Boundary Layer," *AIAA Journal*, Vol. 30, No. 1, 1992, pp. 49–55.

[28] Liu, J., Piomelli, U., and Spalart, P. R., "Interaction Between a Spatially Growing Turbulent Boundary Layer and Embedded Streamwise Vortices," *Journal of Fluid Mechanics*, Vol. 326, Nov. 1996, pp. 151–179.

[29] Cottin, C., and Leweke, T., "Experiments on Vortex Pair Dynamics in Ground Effect," *6th EUROMECH Fluid Mechanics Conference*, Vol. 1, 2006, p. 199, https://www.mech.kth.se/efmc6/web_vol1.pdf.

[30] Duponcheel, M., Cottin, C., Daeninck, G., Leweke, T., and Winckelmans, G., "Experimental and Numerical Study of Counter-Rotating Vortex Pair Dynamics in Ground Effect," *18th congrès français de Mécanique*, CFM Paper 2007-1131, 2007.

[31] Benjamin, T., "Theory of the Vortex Breakdown Phenomenon," *Journal of Fluid Mechanics*, Vol. 14, No. 4, Dec. 1962, pp. 593–629.

[32] Sarpkaya, T., "Effect of the Adverse Pressure Gradient on Vortex Breakdown," *AIAA Journal*, Vol. 12, No. 5, May 1974, pp. 602–607.

[33] Sarpkaya, T., "Vortex Breakdown and Turbulence," *33rd AIAA Aerospace Sciences Meeting and Exhibit*, AIAA Paper 1995-433, 1995.

[34] Leibovich, S., "The Structure of Vortex Breakdown," *Annual Review of Fluid Mechanics*, Vol. 10, No. 1, 1978, pp. 221–246.

[35] Ruith, M. R., Chen, P., Meiburg, E., and Maxworthy, T., "Three-Dimensional Vortex Breakdown in Swirling Jets and Wakes: Direct Numerical Simulation," *Journal of Fluid Mechanics*, Vol. 486, June 2003, pp. 331–378.

[36] Lucas, M., "Influence du sillage de l'installation motrice sur un écoulement d'extrados en configuration de vol de basse vitesse et de forte incidence. Recherche de stratégies de contrôle de l'écoulement," Ph.D. Thesis, Institut Supérieur de l'Aéronautique et de l'Espace, Toulouse, France, 2014.

[37] Lucas, M., Bury, Y., Joly, L., and Bonnaud, C., "Experimental and Computational Investigation of a Simplified Geometry of an Engine/Pylon/Wing Installation at High-Lift Flight Conditions," *Proceedings of the ASME 2013 Fluids Engineering Summer Meeting FEDSM2013*, ASME Paper FEDSM2013-16073, New York, 2013, p. V01BT14A004. https://doi.org/10.1115/FEDSM2013-16073

[38] Lucas, M., Bury, Y., Joly, L., and Bonnaud, C., "Experimental and Computational Analysis of the Flow Past a Simplified Model of an Engine/Pylon/Wing Installation at Low Speed/Moderate Incidence Flight Conditions," *50th 3AF International Conference on Applied Aerodynamics*, 2015.

[39] Cambier, L., and Gazaix, M., "elsA: An Efficient Object-Oriented Solution to CFD Complexity," *Proceedings of the 40th Aerospace Science Meeting and Exhibit (AIAA)*, AIAA Paper 2002-108, 2002.

[40] Menter, F. R., "Two-Equation Eddy-Viscosity Turbulence Models for Engineering Applications," *AIAA Journal*, Vol. 32, No. 8, 1994, pp. 1598–1605. https://doi.org/10.2514/3.12149

[41] Jeong, J., and Hussain, F., "On the Identification of a Vortex," *Journal of Fluid Mechanics*, Vol. 285, No. 1, 1995, pp. 69–94. https://doi.org/10.1017/S0022112095000462

[42] Ting, L., and Klein, R., *Viscous Vortical Flows*, Lecture Notes in Physics 374, Springer–Verlag, Berlin, 1991, pp. 78–103. https://doi.org/10.1002/zamm.19920721210

[43] Hoang, N. T., "The Hemisphere-Cylinder at an Angle of Attack," Ph.D. Dissertation, Dept. of Engineering Science and Mechanics, Virginia Polytechnic Inst. and State Univ., Blacksburg, VA, 1991.

[44] Pauley, W. R., and Eaton, J. K., "Experimental Study of the Development of Longitudinal Vortex Pairs Embedded in a Turbulent Boundary Layer," *AIAA Journal*, Vol. 26, No. 7, 1988, pp. 816–823. https://doi.org/10.2514/3.9974

P. G. Tucker
Associate Editor